

Optimization of muonium yield in perforated silica aerogel

Shihan Zhao¹ and Jian Tang^{1*}

School of Physics, Sun Yat-sen University, Guangzhou 510275, China

 (Received 30 December 2023; accepted 19 March 2024; published 18 April 2024)

A muonium consists of a positive muon associated with an orbital electron, and the spontaneous conversion to antimuonium serves as a clear indication of new physics beyond the Standard Model in particle physics. One of the most important aspects in muonium-to-antimuonium conversion experiment is to increase the muonium yield in vacuum to challenge the latest limit obtained in 1999. This study focuses on a simulation of the muonium formation and diffusion in the perforated silica aerogel. The independent simulation results can be well-validated by experimental data. By optimizing the target geometry, we find a maximum muonium emission efficiency of 7.92(2)% and a maximum vacuum yield of 1.134(2)% with a typical surface muon beam, indicating a 2.6 times and a 2.1 times enhancement, respectively. Our results will pave the way for muonium experiments.

DOI: [10.1103/PhysRevD.109.072012](https://doi.org/10.1103/PhysRevD.109.072012)

I. INTRODUCTION

Muonium, a pure leptonic bound state ($M = \mu^+e^-$), is an ideal subject in precision measurement of the Standard Model and a sensitive probe to new physics beyond SM. Improving the yield of vacuum muonium will make significant contributions in muonium spectroscopy [1–5], precise measurement of muon $g-2$ and electric dipole moment (EDM) [6–8], testing antimatter gravity such as the muonium antimatter gravity experiment (MAGE) [9,10] and the LEMING experiment [11,12], and the search for muonium-to-antimuonium conversion [13–16]. No experiments have investigated this conversion since 1999, with the current conversion probability limit set at $P_{\overline{M}M} < 8.3 \times 10^{-11}$ (90% C.L.) [17]. Recently, we proposed a new muonium-to-antimuonium conversion experiment (MACE) aiming at improving the sensitivity to the spontaneously charged lepton flavor-violating conversion process ($M \rightarrow \overline{M}$, or $\mu^+e^- \rightarrow \mu^-e^+$) by more than two orders of magnitude [18,19]. MACE is designed to search for the rare process by distinguishing the charge and kinematic properties of the decay products between muonium and antimuonium, where only vacuum muonium conversion events are of great interest. Muonium-related experiments can benefit significantly from the increased vacuum muonium yields.

In the production of vacuum muonium, a muon injected into a specific target material may spontaneously capture an electron to compose a muonium atom. After that, some of produced muonium atoms would eventually escape from the material and emit into a vacuum. The target material is chosen to be porous and inactive, such as silica powder or silica aerogel; as a matter of fact, silica powder was used in the latest experiment searching for muonium-antimuonium conversion [17]. In comparison, silica aerogel shares the similar composition but takes a rich porous mesostructure, suitable for the muonium target. Early in 1992, silica aerogel's muonium emission efficiency was measured for the first time, and the result was comparable to that of the silica powder [20], suggesting its potential superiority. After 30 years, a new measurement demonstrated statistically that up to 3 muonium atoms could emit into vacuum for every 1,000 muons stopped [21]. Keep in mind that most of the muonium atoms formed in the material are still trapped [21–24]. There remains a plenty of room for improvement in the muonium emission into a vacuum and a new approach is expected.

Beer *et al.* proposed a laser-ablation method aimed at increasing the muonium emission efficiency. In this approach, an aerogel target is ablated with a femtosecond pulsed laser so that the target surface at the beam downstream side is perforated (Fig. 1) [25]. The laser ablates nearly cylindrical holes with diameters ranging from tens to hundreds of micrometers and depths of a few millimeters. These holes are arranged in an equilateral triangular lattice perpendicular to the surface of the target, spaced tens to hundreds of micrometers apart. This perforated structure significantly enhances muonium diffusion and substantially increases its vacuum yield. Multiple ablation structure parameters were tested in TRIUMF and an emission efficiency of up to 2% was achieved, indicating an order

*tangjian5@mail.sysu.edu.cn

Published by the American Physical Society under the terms of the [Creative Commons Attribution 4.0 International license](https://creativecommons.org/licenses/by/4.0/). Further distribution of this work must maintain attribution to the author(s) and the published article's title, journal citation, and DOI. Funded by SCOAP³.

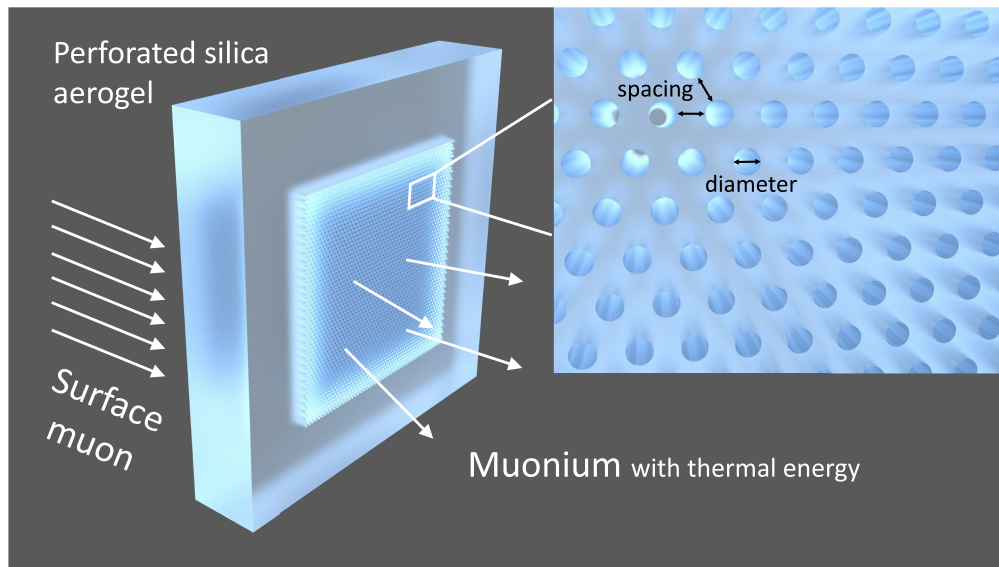


FIG. 1. The schematic diagram of muonium emission in the silica aerogel target.

of magnitude improvement [24]. The authors also attempted to reveal the emission mechanism of muonium by proposing and analyzing the opening fraction, a characteristic parameter, to figure out the dependency of muonium emission efficiency. However, the latest results roughly showed a positive correlation between the opening fraction and yield while more complex dependencies remained blank. The insufficient number of samples also led to an incomplete understanding of the underlying mechanism. In addition to the experiments conducted at TRIUMF, measurements on muonium emission efficiency in perforated aerogel were also conducted in PSI [26]. In the PSI experiment, a slow muon beam ($p_{\mu^+} = 11\text{--}13\text{ MeV}/c$) entered the front surface of the aerogel sample, and muonium atoms were emitted into vacuum upstream. However, the emission efficiency depends on the emission model parameters, and further discussion about the enhancement of perforated structures on muonium emission is lacking. We also note that an independent simulation study was carried out to model the muonium diffusion in silica aerogel and was applied to a novel multilayer target design [27]. They modeled the transport of muonium as a diffusion process with a thermal momentum distribution. However, they incorporated the effect from enlarged diffusion constants while detailed considerations of perforated structures remained unrevealed.

In this study, we model muonium diffusion as a three-dimensional off-lattice thermal random walk and propose a new muonium tracking algorithm that comprehensively considers the perforated structure. We simulate the muonium diffusion inside perforated silica aerogel with the measured mean free path rather than fitting the diffusion constant, so that we carry out the first explicit dependency of the muonium yield on the perforation parameters. Furthermore, the simulation method is validated and

applied to a muonium yield optimization. This study will further guide the development and optimization of the muonium target, and pave the way for the design and optimization of MACE. Our method could benefit the precision measurement and the search for new physics in the muon sector, the development on cutting-edge muon spin relaxation/rotation/resonance (μSR) techniques [28–32], the positronium physics and technologies, including the positronium production and emission [33–36], positronium spectroscopy and annihilation [37–40], anti-hydrogen gravity experiment (AEGIS) [34,41,42], and positron emission tomography (PET) [43].

This article is organized as follows. In Sec. II, the theoretical formalism and the simulation method are described. In Sec. III, we present the validation of the simulation. We then apply the new algorithm to optimize the vacuum muonium yield in Sec. III. The findings of this work are finally summarized in Sec. V.

II. MUONIUM DIFFUSION AND ITS SIMULATION

Silica aerogel is an inactive porous material with a rich mesostructure. It is a matter similar to common gels, but the liquid component is replaced by gas, which makes its porosity extremely high (80%–99.8%) but density extremely low ($\mathcal{O}(10)\text{ mg}/\text{cm}^3$) [44–46]. Microscope photos demonstrate that a silica aerogel has a complex network structure, with a characteristic scale of tens to hundreds of nanometers. The silica network structure allows molecules or atoms to diffuse inside the intergranular void [47].

If the aerogel is placed in vacuum for a sufficient period, air molecules inside would diffuse and come out of the material. This allows muonium to move freely within the intergranular voids until it collides with silica. After a collision at room temperature, muonium will mostly be

inelastically scattered instead of being captured, which is supported by the direct measurement of reflection probability from the silica surface [48]. Significant absorption only takes place when it is far below room temperature [23]. Furthermore, density functional theory (DFT) calculations of hydrogen atom dynamics inside silica [49] and independent measurements on hydrogen absorption by silica aerogel [50] also support this proposition. Therefore, muonium atoms experience a series of scattering in silica aerogel before decaying and thus can be effectively modeled as a three-dimensional off-lattice random walk. In the random walk model, we assume that:

- (i) Inside the aerogel, muonium atoms move freely between any two successive scatterings on silica described by Eq. (1), and the distribution of the free path is an exponential distribution with a mean free path depending on the structure of the aerogel given by Eq. (2).
- (ii) Each scattering changes the momentum of muonium atoms, and the velocity distribution after scattering follows a Maxwell distribution in Eq. (3). It is inferred from the assumption that the system has reached a specific thermal equilibrium [51], and the kinetic energy of muonium atoms follows a Boltzmann distribution.

Following this principle, a recursive equation of motion describing a muonium atom inside a silica aerogel can be written as

$$\begin{aligned}\Delta t_i &= \frac{r_i}{v_i}, \\ t_{i+1} &= t_i + \Delta t_i, \\ \mathbf{x}_{i+1} &= \mathbf{x}_i + \mathbf{v}_i \Delta t_i,\end{aligned}\quad (1)$$

where (t_i, \mathbf{x}_i) , r_i , \mathbf{v}_i , and $v_i = \|\mathbf{v}_i\|$ are the spacetime coordinates, the free path, the velocity and the velocity magnitude at the i th step, respectively. Both r_i and \mathbf{v}_i are random variables sampled from the corresponding distribution at each step. Considering the randomly connected network structure in a silica aerogel, it is convinced that the free path follows an exponential distribution with a parameter λ ,

$$f_r(r) = \frac{1}{\lambda} \exp\left(-\frac{r}{\lambda}\right), \quad (2)$$

where $\lambda = \langle r \rangle$ is the mean free path. The magnitude of λ is positively correlated with the size of mesocavities inside the aerogel.

It comes to the velocity distribution now. Inside an aerogel, muonium atoms experience a series of inelastic scattering on silica structures, and the emission velocity distribution after scattering is related to the interaction between the muonium atoms and silica [49,51,52]. Therefore, in principle, the exact distribution should be

determined by experimental data or *ab initio* calculations. As an approximation, it is believed that the ensemble of muonium atoms and target molecules quickly reaches the thermal equilibrium [51]. Therefore, the kinetic energy of muonium atoms should follow the form of the Boltzmann distribution, and the velocity distribution takes the form

$$f_v(\mathbf{v}) = \left(\frac{m_M}{2\pi k_B T_{\text{eff}}}\right)^{3/2} \exp\left(-\frac{m_M v^2}{2k_B T_{\text{eff}}}\right), \quad (3)$$

where m_M is the mass of muonium, k_B is the Boltzmann constant and T_{eff} is the effective temperature. It is known that the room temperature will overestimate the muonium decay time. One of the interpretation is the underestimation of kinetic energy. We can always correct the effect by elevating the temperature [21,27]. The experimental work of Antognini *et al.* found the temperature to be 400 K by considering a simplified emission model with a given diffusion time $\Delta t_{\text{diff}} = 200$ ns [26]. However, their emission model has correlations between Δt_{diff} and temperature. Therefore, the temperature depends on the choice of Δt_{diff} . Another simulation study presented by Ce Zhang *et al.* estimated the temperature to be around 320 K (320 ± 2 K for flat target and 322 ± 2 K for perforated target) with datasets measured at TRIUMF. In the model, the diffusion time is naturally included and the temperature is determined by data fitting. In our study, we choose $T_{\text{eff}} = 322$ K to perform the following simulations. Equations (1)–(3), as an iterative scheme of the special off-lattice random walk, simulates the motion of muonium until it reaches the material surface or decays.

To perform accurate simulations in a perforated structure, it is also important to track muonium outside the material reliably. The commonly used method for navigating and tracking particles in a complex geometry is to calculate the geometric relations between particles and the voxelized geometry (e.g., GEANT4 [53–55]). However, this method can hardly handle a perforated target with tens of thousands of micro holes, since neither the full geometry can be easily constructed nor an efficient navigation or tracking can be performed. Therefore, an alternative method is needed. Our solution is to use a combinatorial tracking method. The voxelized geometry-based tracking method controls muonium motion outside the target bounding box while a Boolean-expression-based tracking method controls muonium motion inside. This combination can resolve the realizability and performance issues raised in the voxelized-geometry-based tracking method.

To implement the method, the first question is how to describe the target full geometry in the combinatorial tracking system. The solution involves a Boolean expression to describe the perforated structure and a bounding box (a GEANT4 volume) to describe the target region where the Boolean expression should be enabled. The Boolean expression divides the target volume into two different

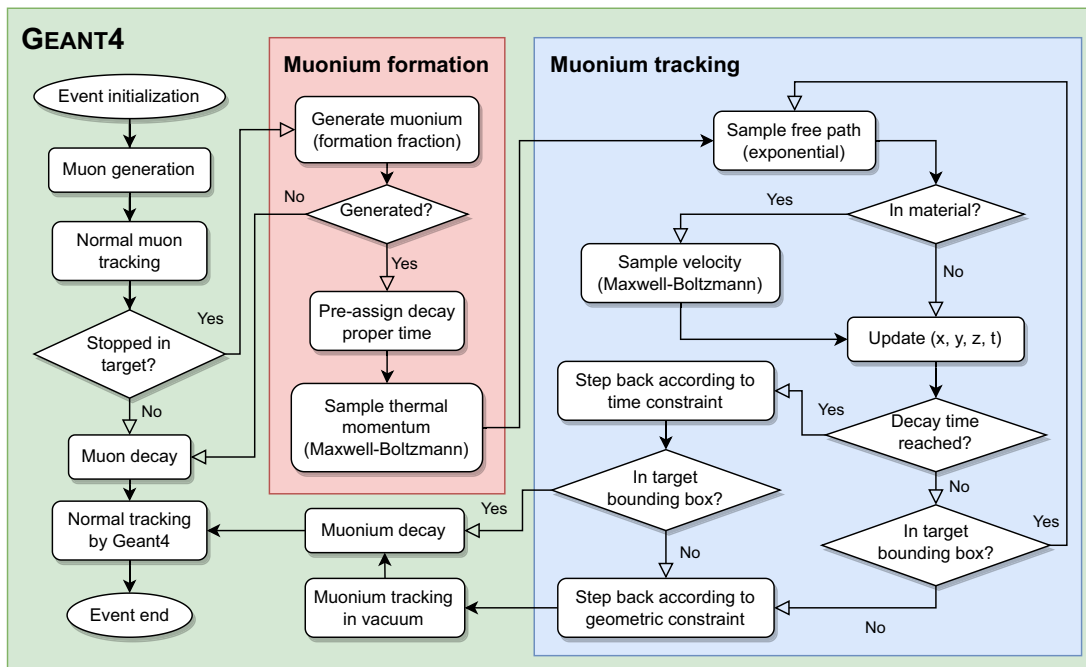


FIG. 2. The muonium formation and tracking algorithm in the simulation.

subregions; a `true` region representing the material where muonium atoms follow the random walk, and a `false` region representing the vacuum where muonium atoms move freely. During each step of the random walk, the Boolean expression is calculated to determine the inclusion of the muonium in the material and the state of motion. If a muonium atom appears inside the material, a free path and a velocity are sampled and the spacetime coordinates are updated. Otherwise, only a free path is sampled and the state of motion is updated with the current velocity. The process will loop until any of the termination conditions, i.e., the muonium decays or escapes from the target bounding box, is triggered. Then the Boolean-expression-based tracking comes to an end and the tracking procedure is returned to the voxelized-geometry-based method (GEANT4). The muonium formation and tracking algorithm in the simulation is shown in Fig. 2.

This combinatorial tracking method combines the power of GEANT4 and the Boolean-expression-based algorithm in the same procedure, allowing us to successively simulate a muon track and a muonium track. We are able to simulate the dependency of the muonium yield with regards to different muon beam conditions conveniently and precisely, so that the approach can be validated with experimental data. The large-scale simulation can be performed in a local supercomputer following the software deployment strategy in Ref. [56].

III. VALIDATION OF SIMULATION SCHEME

After a discussion of how to simulate the muonium diffusion in a perforated target, this section demonstrates a

validation of the simulation method. The previous experimental studies, utilizing aerogel targets with many tiny blind holes arranged in an equilateral triangular lattice at the downstream surface, have accumulated vacuum muonium production data in different experimental setups. Two datasets can be used for the validation; one is the vacuum muonium yield data [24], and the other is the spacetime distribution of muonium decays [21,25]. Simulations will be performed and corresponding datasets will be derived by analyzing the simulation data.

The model described in Sec. II contains two free parameters; a mean free path λ and a temperature T . While the temperature is chosen to be 322 K according to the previous fit [27], the mean free path is estimated by the empirical scaling formula $\lambda = \lambda_0(\rho_0/\rho)^{1.5}$ [21]. The reference mean free path λ_0 and the reference target density ρ_0 are 226 nm and 29 mg/cm³, respectively. Since the target densities involved in this validation are close to the reference values, the scaling formula can be applied. The perforated structure is simplified as cylindrical blind holes arranged in an equilateral triangular pattern, with its axis perpendicular to the target surface, as shown in Fig. 1. This structure is represented completely by a Boolean expression and a target bounding box (GEANT4 `G4BOX`). The spacing, diameter, and depth of the holes are geometric parameters kept the same as the experiment. The remaining simulation settings are also kept the same as the corresponding benchmark experiment.

We first validate the spacetime distribution of muonium decay by comparing it with measurements in TRIUMF [21,25]. In the simulation, a $\sigma_{xy} = 5$ mm

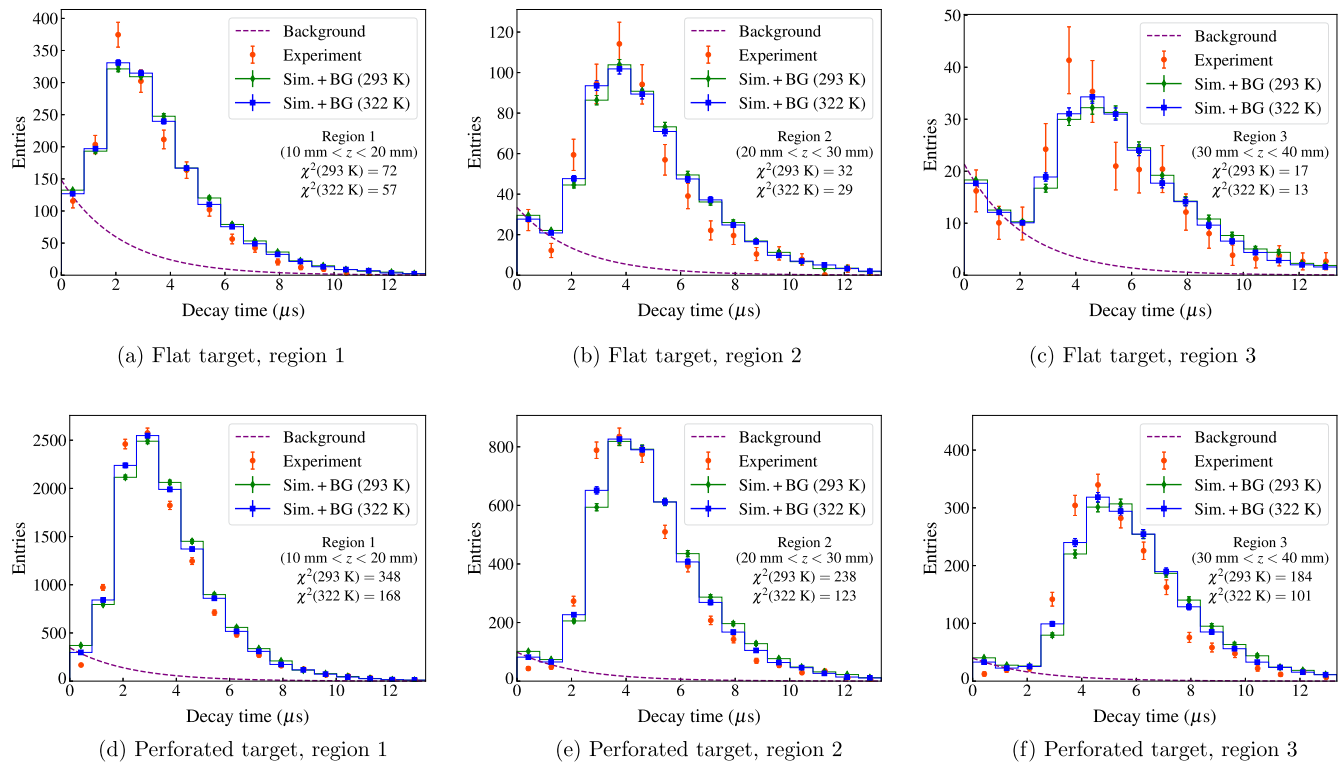


FIG. 3. The spacetime distribution of muonium decay. The simulation histogram and an exponential muon decay background are fit to the experimental histogram.

Gaussian profiled collimated surface muon beam carrying 22.9 MeV/ c momentum with 1.5% spread (rms) is incident on the target. The target thickness is 6.9 mm and perforated by 270 μm diameter and 30 μm spacing holes, from which some of the muonium atoms emit into the surrounding vacuum and decay. These decays are divided into three different space regions ranging from $z = 10$ mm to 40 mm, as shown at the simulation results in Fig. 3. Simulated-decay z positions are Gaussian smeared by 2 mm (rms), according to the experiment. The simulated distribution and an exponential muon decay background are fitted to the experimental histogram. A room temperature (293 K) and an elevated temperature (322 K, according to Zhang's fit [27]) are used in the simulation. The result shows agreement between simulation and experiment with $\chi^2(322 \text{ K}) < \chi^2(293 \text{ K})$ for all cases, as we mentioned above. Although the overall shape is well-replicated by the simulation, the values of χ^2 indicate systematic errors in the simulated decay spacetime distribution. The suboptimal temperature is account for most of systematic errors, and, in fact, the goodness of fit can be improved by further tuning the temperature, which is crucial for precision measurement experiments in real cases. However, our primary goal is to simulate the vacuum yield of the perforated target, and one might question whether the difference in the decay spacetime distribution will significantly affect the yield

result. We will answer it by a second round of validation on the muonium emission efficiency into vacuum.

We now simulate vacuum muonium emission efficiency of perforated targets with different ablation schemes (S01, S04, S05, S09–S13, S18–S20, and S23 in Ref. [24]) and compare them with measurement results in TRIUMF [24]. The simulation setup follows the experiment. In the simulation, a collimated surface muon beam with 23 MeV/ c momentum and 2% momentum spread (rms) hits the target with a Gaussian profile of $\sigma_{xy} = 5$ mm. A plastic scintillator is placed at $z = -12$ mm, with 40 mm width and 380 μm thickness. The target geometry is identical to the experiment and its downstream surface is placed at $z = 0$. Muonium decays at $z > 0$ are counted, and are used to calculate muonium emission efficiency by a ratio of the number of muonium decays in vacuum over the number of decays in the target. The simulation results are presented in Fig. 4, and errors between the simulation and the experiment are mostly within 20%, indicating a certain agreement. The significant deviations in the samples (S01, S04, S05, and S18) are currently not well-explained. One of the possible reason might be related the deformation of the real target samples, which can hardly covered in the simulation. We tend to consider the deviations as the systematic errors, which will not affect the reliability of the simulation. In conclusion, the straightforward simulations now can describe the transport of muonium well in complex aerogel geometry and provide

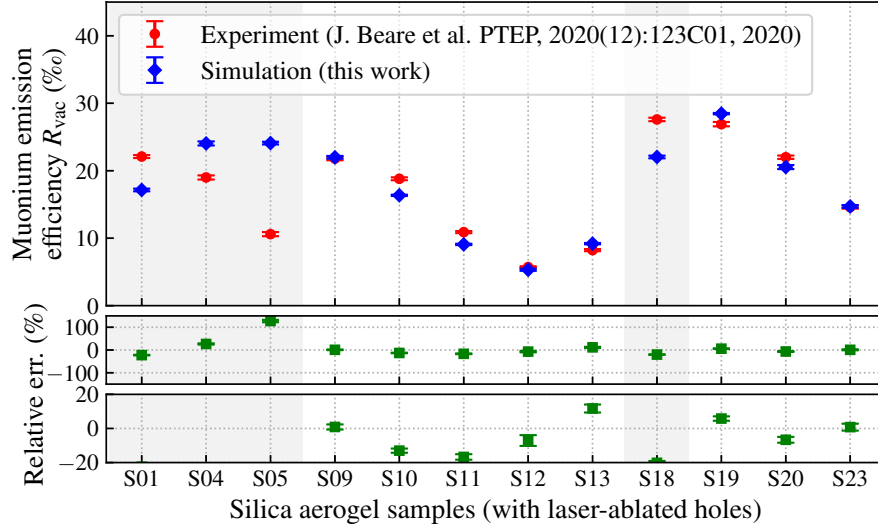


FIG. 4. A comparison of muonium emission efficiency in simulation and experiment.

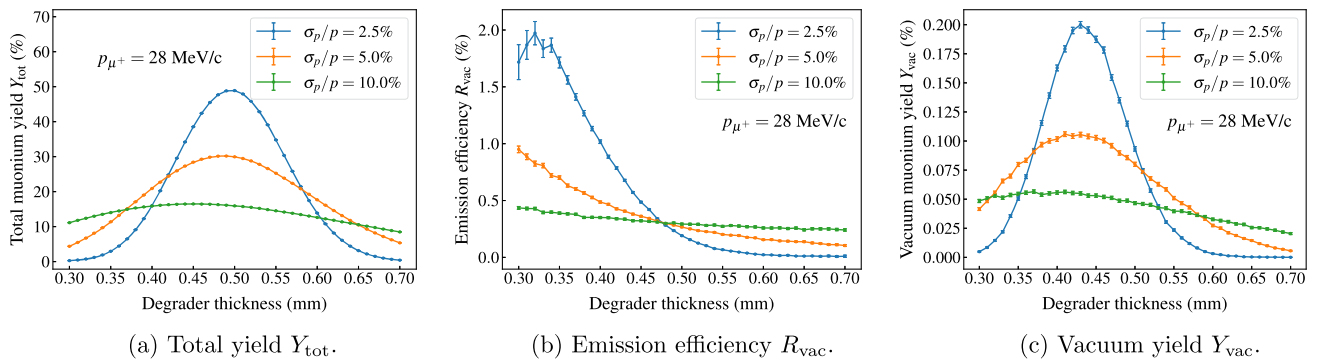
reasonable yield estimations. Precision measurement experiments might need calibrated simulations in detail.

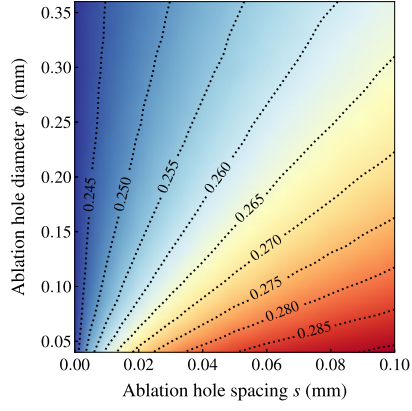
IV. SIMULATION-GUIDED YIELD OPTIMIZATION

With the simulation method validated, we can utilize it to investigate the performance of perforated targets of different ablation configurations to guide the optimization of the mainstream scheme in the related muonium experiment. In this section, we will study the muonium yield under various target geometries to find the dependencies of muonium yield on key parameters. The perforation structure is the same as Fig. 1, with a target size of $60 \text{ mm} \times 60 \text{ mm} \times 10 \text{ mm}$ and ablation holes with different geometric parameters in the $40 \text{ mm} \times 40 \text{ mm}$ area at the center of the downstream surface. These geometric parameters include a hole spacing of $0\text{--}100 \text{ }\mu\text{m}$, a diameter of $40\text{--}360 \text{ }\mu\text{m}$, and depths of 1 mm , 2 mm , and 5 mm . The temperature is set to 322 K as the same in previous sections. Three kinds of surface muon beams carrying $28 \text{ MeV}/c$ momentum with momentum

spread of 2.5% , 5% , and 10% are considered. In a real experiment, the muon beam usually passes materials such as a beam degrader or a beam monitor [57]. Therefore, we place an aluminum degrader at 5 mm in front of the target where the muon beam goes through and loses energy. A portion of muons will stop in the target and form muonium atoms. The degrader with a different thickness will result in various distributions for muon stopping positions. Thereby, the degrader can affect the emission of muonium into vacuum and eventually change the vacuum yield. It means that the degrader thickness should be optimized to achieve the maximum yield, as shown in simulation results Fig. 5. From the results, we infer the optimal degrader thicknesses for beam momentum spread of 2.5% , 5% , and 10% are $430 \text{ }\mu\text{m}$, $410 \text{ }\mu\text{m}$, and $370 \text{ }\mu\text{m}$, respectively.

We use five quantities, $f_{\mu^+}^{\text{stop}}$, f_M , Y_{tot} , R_{vac} , and Y_{vac} , to characterize the formation and emission of muonium. They represent the muonium formation fraction, the muon stopping fraction, the total muonium yield, the muonium emission efficiency, and the vacuum muonium yield, respectively. They are defined as


 FIG. 5. Muonium production and emission from a flat silica aerogel target with different aluminium degraders ($t_{\text{target}} = 10 \text{ mm}$, $\rho_{\text{target}} = 30 \text{ mg}/\text{cm}^3$, $\lambda = 200 \text{ nm}$, and $T = 322 \text{ K}$).



(a) Total muonium yield Y_{tot}
 $(\sigma_p/p = 2.5\%, d = 1 \text{ mm})$

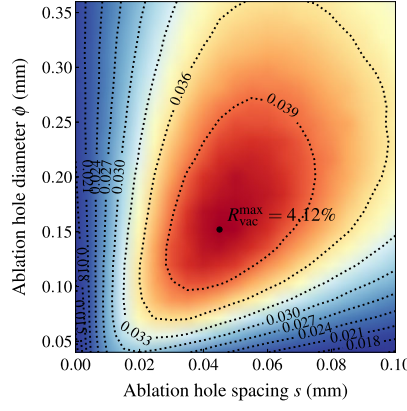


TABLE I. Simulation of maximum muonium emission efficiency and corresponding optimal spacing and diameter with different beam condition.

Data	p_{beam} (MeV/c)	$\sigma_{p_{\text{beam}}}/p_{\text{beam}}$ (%)	Depth d (mm)	Spacing s (μm)	Diameter ϕ (μm)	Max emission efficiency R_{vac} (%)
Simulation ^a	2.5		1	45 ± 5	152 ± 16	4.124 ± 0.007
			2	50 ± 5	232 ± 16	4.980 ± 0.009
			5	35 ± 5	360 ± 16	7.92 ± 0.02
	28	5	1	50 ± 5	168 ± 16	2.762 ± 0.007
			2	50 ± 5	248 ± 16	3.172 ± 0.008
			5	40 ± 5	312 ± 16	4.36 ± 0.01
	10		1	50 ± 5	152 ± 16	2.166 ± 0.007
			2	50 ± 5	232 ± 16	2.451 ± 0.008
			5	45 ± 5	312 ± 16	3.22 ± 0.01
Ref. [24] (S18) ^a	23	2	1	85	165	2.76 ± 0.02^b
Ref. [25] ^b	28	5	4.75 ± 0.25	30	270	3.05 ± 0.03^b
Ref. [26] (Aerogel-1)	12.5	3.4	4.5 ± 0.5	45 ± 5	105 ± 5	$6.72 \pm 0.05_{-0.76}^{+1.06c}$

^aOnly statistical errors are shown.

^bIncludes muonium decays within $10 \text{ mm} < z < 40 \text{ mm}$ only.

^cModel-dependent assumptions of the temperature at 400 K and the diffusion time at 200 ns.

However, the vacuum muonium yield Y_{vac} is comprised of R_{vac} and $f_{\mu^+}^{\text{stop}}$, so the geometry dependence of Y_{vac} is more complex. On one hand, increasing the spacing between holes will increase the total amount of material, thereby increasing the rate of muons stopping in the material and producing muonium, but these muonium atoms are less likely to emit into vacuum due to the material's obstruction. On the other hand, increasing the diameter of the hole can improve the emission efficiency, but this will reduce the overall muonium yield. Therefore, it can be expected that there is a geometric parameter combination that leads to the highest vacuum yield when the material and the beam condition are fixed. The simulation results support this prospect. As shown in Fig. 6, there exists a maximum value for both vacuum yield and emission efficiency. As the spacing and diameter deviate from the optimal values, the vacuum yield and emission efficiency gradually drop and are significantly suppressed when the spacing or diameter is too tiny.

Based on the notable relation $Y_{\text{vac}} = R_{\text{vac}} f_{\text{M}} f_{\mu^+}^{\text{stop}}$, the enhancement in muonium vacuum yield Y_{vac} can be achieved by three different mechanisms:

- (i) Enhancement by sufficient open surface area that enhances muonium diffusion towards vacuum, which contributes positively to R_{vac} . This enhancement is suppressed when the diameter is too small or the spacing is too large, as shown in Fig. 6. In this case, although muonium atoms are formed near the target surface, there is little opening surface for them to easily diffuse into the vacuum. Meanwhile, they have a long distance to travel before leaving the material, during which

most of them decay and cannot reach the target surface.

- (ii) Enhancement by favorable forming position. In this case, muoniums originate near the target surface and is favorable for their emission into vacuum, which contributes positively to R_{vac} . This enhancement is suppressed when the spacing is tiny, as shown in Fig. 6, or the beam momentum spread is large, as shown in Table I and Table II. For tiny spacings, muonium tends to form near the bottom of the hole rather than near the target surface, since there is not enough material to support sufficient muonium formation near the surface. For large beam momentum spread, the distribution of muonium forming position tends to be uniform, with a large number of muoniums produced deep inside the target. Both of these two situations require a long diffusion path for muonium atoms to travel before they emit into vacuum.
- (iii) Enhancement by appropriate material removal, which contributes positively to Y_{tot} . This mechanism takes effect when materials are not excessively removed (i.e., with large spacing or small diameter, as shown in Fig. 6). At this point, there are more muons stopped inside the target so the original total yield of muonium is higher, leading to a higher vacuum yield.

In conclusion, we prefer to have a high-quality muon beam with minimize momentum spread and an appropriate opening surface area, which can maximize the number of muonium atoms forming near the target surface and maximize the muonium emission into vacuum. This guides us to optimize the muonium target in MACE.

TABLE II. Simulation of maximum vacuum muonium yield and corresponding optimal spacing and diameter with different beam condition.

Data	p_{beam} (MeV/c)	$\sigma_{p_{\text{beam}}}/p_{\text{beam}}$ (%)	Depth d (mm)	Spacing s (μm)	Diameter ϕ (μm)	Max vacuum yield Y_{vac} (%)
Simulation ^a		2.5	1	50 ± 5	152 ± 16	1.092 ± 0.002
			2	55 ± 5	184 ± 16	1.134 ± 0.002
			5	55 ± 5	184 ± 16	1.122 ± 0.002
	28	5	1	50 ± 5	152 ± 16	0.583 ± 0.001
			2	60 ± 5	216 ± 16	0.607 ± 0.001
			5	50 ± 5	184 ± 16	0.604 ± 0.001
		10	1	50 ± 5	152 ± 16	0.305 ± 0.001
			2	55 ± 5	200 ± 16	0.320 ± 0.001
			5	60 ± 5	232 ± 16	0.321 ± 0.001
	Ref. [24] (S18) ^a	23	2	1	85	165
Ref. [25] ^a	28	5	4.75 ± 0.25	30	270	$0.265 \pm 0.003^{\text{b,c}}$
Ref. [26] (Aerogel-1) ^a	12.5	3.4	4.5 ± 0.5	45 ± 5	105 ± 5	$1.22 \pm 0.01^{\text{b,d}}$

^aOnly statistical errors are shown.

^bConverted from R_{vac} (Table I) by $Y_{\text{vac}} = R_{\text{vac}} f_{\text{M}} f_{\mu^+}^{\text{stop}}$, assuming $f_{\mu^+}^{\text{stop}} = \frac{1}{2} \left(1 - \frac{\pi(\phi/2)^2}{\sqrt{3}/2(s+\phi)^2}\right)$ by considering muons are half-stopped in flat target and taking into account the material volume fraction near the surface after ablation, and $f_{\text{M}} = 0.655$ [24].

^cIncludes muonium decays within $10 \text{ mm} < z < 40 \text{ mm}$ only.

^dModel-dependent assumptions of the temperature at 400 K and the diffusion time at 200 ns.

V. SUMMARY AND OUTLOOK

We have developed a technique to simulate the muonium production and tracking in perforated silica aerogel, and implemented it in GEANT4 as an independent physical process. This simulation technique has been validated with the spacetime distribution in muonium decays and the muonium emission efficiency measured in TRIUMF. The validation has shown a good consistency between simulation and experiment. In addition, optimization of geometric parameters in the perforated aerogel has been carried out so that we could make good use of the simulation technique to facilitate muonium-related experiments such as MACE. We have considered a simplified simulation setup based on real experimental circumstances and incident beams under different conditions to investigate the performance of different target geometries. We have scanned the depth, spacing, and diameter of the holes within a certain range and, for the first time, have determined the explicit dependency of the total muonium yield, the muonium emission efficiency, and the vacuum muonium yield on the geometric parameters. We have identified the mechanisms for the enhancement of vacuum muonium yield in the experimental design and possible optimization directions are indicated. Nevertheless, there is still plenty of room for further improvement in the simulation techniques and muonium targets. On one hand, in the simulation technique, the effect of material removal caused by laser ablation on the muon transportation has not been considered in detail due to the independence of the

current process implementation, and the meticulous combination of this muonium tracking process with the muonium conversion process or other muonium-related processes inside the material is still a technical topic needs to be studied. On the other hand, it is convinced that the combination of a low-momentum-spread muon beam and an optimized target will lead to higher muonium yields in a vacuum, which deserves further investigation. We believe that this new simulation method can inspire novel target designs and help achieve better results. It could be expected that our simulation technique will make an essential contribution to the optimization and guidance of muonium target design and will pave the way for the related science and technology frontiers, which share similar hydrogenlike atom formation and diffusion physics.

ACKNOWLEDGMENTS

We express our gratitude to Dr. Ce Zhang and Professor Dr. Tsutomu Mibe for fruitful discussions. We also appreciate the great efforts made by the MACE working group. Our thanks also go to Ruixuan Gao for her meticulous proofreading efforts. This project was supported in part by the National Natural Science Foundation of China under Grant No. 12075326, the Natural Science Foundation of Guangzhou under Grant No. 2024A04J6243 and Fundamental Research Funds for the Central Universities (23xkjc017) in Sun Yat-sen University. The simulation was conducted by a strong support of computing resources from the National Supercomputer Center in Guangzhou.

- [1] S. Kanda *et al.*, New precise spectroscopy of the hyperfine structure in muonium with a high-intensity pulsed muon beam, *Phys. Lett. B* **815**, 136154 (2021).
- [2] S. Nishimura *et al.* (MuSEUM Collaboration), Rabi-oscillation spectroscopy of the hyperfine structure of muonium atoms, *Phys. Rev. A* **104**, L020801 (2021).
- [3] B. Ohayon *et al.* (Mu-MASS Collaboration), Precision measurement of the Lamb shift in Muonium, *Phys. Rev. Lett.* **128**, 011802 (2022).
- [4] G. Janka *et al.*, Measurement of the transition frequency from $2S_{1/2}$, $F = 0$ to $2P_{1/2}$, $F = 1$ states in Muonium, *Nat. Commun.* **13**, 7273 (2022).
- [5] I. Cortinovis, B. Ohayon, L. de Sousa Borges, G. Janka, A. Golovizin, N. Zhadnov, and P. Crivelli, Update of Muonium $1S-2S$ transition frequency, *Eur. Phys. J. D* **77**, 66 (2023).
- [6] H. Iinuma (J-PARC muon $g-2$ /EDM Collaboration), New approach to the muon $g-2$ and EDM experiment at J-PARC, *J. Phys. Conf. Ser.* **295**, 012032 (2011).
- [7] Y. Sato (J-PARC E34 Collaboration), J-PARC muon $g-2$ /EDM experiment, *J. Phys. Soc. Jpn. Conf. Proc.* **33**, 011110 (2021).
- [8] M. Otani (J-PARC muon $g-2$ /EDM C Collaboration), Muon $g-2$ /EDM experiment at J-PARC, *Proc. Sci., NuFact2021* (2022) 139.
- [9] A. Antognini, D. M. Kaplan, K. Kirch, A. Knecht, D. C. Mancini, J. D. Phillips, T. J. Phillips, R. D. Reasenberg, T. J. Roberts, and A. Soter (MAGE Collaboration), Studying antimatter gravity with muonium, *Atoms* **6**, 17 (2018).
- [10] D. S. Hajdukovic, Antimatter gravity and the Universe, *Mod. Phys. Lett. A* **35**, 2030001 (2019).
- [11] K. Kirch and K. S. Khaw, Testing antimatter gravity with muonium, *Int. J. Mod. Phys. Conf. Ser.* **30**, 1460258 (2014).
- [12] A. Soter and A. Knecht, Development of a cold atomic muonium beam for next generation atomic physics and gravity experiments, *SciPost Phys. Proc.* **5**, 031 (2021).
- [13] N. Kawamura, R. Kitamura, H. Yasuda, M. Otani, Y. Nakazawa, H. Iinuma, and T. Mibe, A new approach for $\overline{\mu} - \mu$ conversion search, *J. Phys. Soc. Jpn. Conf. Proc.* **33**, 011120 (2021).
- [14] T. Fukuyama, Y. Mimura, and Y. Uesaka, Models of the muonium to antimuonium transition, *Phys. Rev. D* **105**, 015026 (2022).
- [15] J. Heeck and A. Thapa, Zee-model predictions for lepton flavor violation, *Phys. Lett. B* **841**, 137910 (2023).
- [16] Y. Afik, P. S. Bhupal Dev, and A. Thapa, Hints of a new leptophilic Higgs sector?, *Phys. Rev. D* **109**, 015003 (2024).
- [17] L. Willmann *et al.*, New bounds from searching for muonium to anti-muonium conversion, *Phys. Rev. Lett.* **82**, 49 (1999).
- [18] C. Han, D. Huang, J. Tang, and Y. Zhang, Probing the doubly charged Higgs boson with a muonium to antimuonium conversion experiment, *Phys. Rev. D* **103**, 055023 (2021).
- [19] A.-Y. Bai *et al.* (MACE Working Group), Snowmass2021 Whitepaper: Muonium to antimuonium conversion, in 2022 Snowmass Summer Study (2022), [arXiv:2203.11406](https://arxiv.org/abs/2203.11406).
- [20] W. Schwarz, V. Ebert, H. Geerds, K. Jungmann, S. Kirches, S. Koppe, F. Maas, H.-J. Mundinger, G. zu Putlitz, J. Rosenkranz, W. Schäfer, G. Schiff, Z. Zhang, M. Boshier, and V. Hughes, Thermal muonium in vacuo from silica aerogels, *J. Non-Cryst. Solids* **145**, 244 (1992).
- [21] P. Bakule *et al.*, Measurement of muonium emission from silica aerogel, *Prog. Theor. Exp. Phys.* **2013**, 103C01 (2013).
- [22] G. A. Beer *et al.*, Emission of muonium into vacuum from a silica powder layer, *Phys. Rev. Lett.* **57**, 671 (1986).
- [23] A. Antognini *et al.*, Muonium emission into vacuum from mesoporous thin films at cryogenic temperatures, *Phys. Rev. Lett.* **108**, 143401 (2012).
- [24] J. Beare *et al.*, Study of muonium emission from laser-ablated silica aerogel, *Prog. Theor. Exp. Phys.* **2020**, 123C01 (2020).
- [25] G. A. Beer *et al.*, Enhancement of muonium emission rate from silica aerogel with a laser ablated surface, *Prog. Theor. Exp. Phys.* **2014**, 91C01 (2014).
- [26] A. Antognini *et al.*, Room-temperature emission of muonium from aerogel and zeolite targets, *Phys. Rev. A* **106**, 052809 (2022).
- [27] C. Zhang *et al.*, Modeling the diffusion of muonium in silica aerogel and its application to a novel design of multi-layer target for thermal muon generation, *Nucl. Instrum. Methods Phys. Res., Sect. A* **1042**, 167443 (2022).
- [28] K. A. Woodle, K.-P. Arnold, M. Gladisch, J. Hofmann, M. Janousch, K. P. Jungmann, H.-J. Mundinger, G. z. Putliz, J. Rosenkranz, W. Schaefer, G. Schiff, W. Schwarz, V. W. Hughes, and S. H. Kettel, Measurement of the polarization of thermal muonium in vacuum, *Z. Phys. D At. Mol. Clusters* **9** (1988).
- [29] M. H. Dehn, Y. Cao, P.-X. Wang, S. P. Cottrell, M. J. MacLachlan, D. G. Fleming, and R. F. Kiefl, Direct observation of muonium reacting with uncapped gold nanoparticles in porous silica and nature of the final state, *J. Chem. Phys.* **152**, 184706 (2020).
- [30] A. D. Pant, K. Ishida, N. Kawamura, S. Matoba, A. Koda, S. Nishimura, and K. Shimomura, Study of muonium behavior in n-type silicon for generation of ultra cold muonium in vacuum, *Physica (Amsterdam)* **613B**, 412997 (2021).
- [31] A. D. Hillier, S. J. Blundell, I. McKenzie, I. Umegaki, L. Shu, J. A. Wright, T. Prokscha, F. Bert, K. Shimomura, A. Berlie, H. Alberto, and I. Watanabe, Muon spin spectroscopy, *Nat. Rev. Methods Primers* **2**, 4 (2022).
- [32] X. Ni, L. Zhou, M. M. Martins, Z. Salman, A. Suter, and T. Prokscha, Small sample measurements at the low energy muon facility of Paul Scherrer Institute, *Nucl. Instrum. Methods Phys. Res., Sect. A* **1054**, 168399 (2023).
- [33] D. B. Cassidy, P. Crivelli, T. H. Hisakado, L. Liskay, V. E. Meline, P. Perez, H. W. K. Tom, and A. P. Mills, Jr., Positronium cooling in porous silica measured via Doppler spectroscopy, *Phys. Rev. A* **81**, 012715 (2010).
- [34] R. Ferragut, A. Dupasquier, A. Calloni, G. Consolati, F. Quasso, M. P. Petkov, S. M. Jones, A. Galarneau, and F. Di Renzo, Homogeneous porous silica for positronium production in AEGIS, *J. Phys. Conf. Ser.* **262**, 012020 (2011).
- [35] M. Girardi-Schappo, W. Tenfen, and F. Arretche, A random walk approach to the diffusion of positrons in gaseous media, *Eur. Phys. J. D* **67**, 123 (2013).
- [36] A. Deller, B. S. Cooper, T. E. Wall, and D. B. Cassidy, Positronium emission from mesoporous silica studied by

- laser-enhanced time-of-flight spectroscopy, *New J. Phys.* **17**, 043059 (2015).
- [37] L. Gurung, T. J. Babij, S. D. Hogan, and D. B. Cassidy, Precision microwave spectroscopy of the positronium $n = 2$ fine structure, *Phys. Rev. Lett.* **125**, 073002 (2020).
- [38] P. Moskal *et al.*, Testing *CPT* symmetry in ortho-positronium decays with positronium annihilation tomography, *Nat. Commun.* **12**, 5658 (2021).
- [39] G. S. Adkins, D. B. Cassidy, and J. Pérez-Ríos, Precision spectroscopy of positronium: Testing bound-state QED theory and the search for physics beyond the Standard Model, *Phys. Rep.* **975**, 1 (2022).
- [40] R. E. Sheldon, T. J. Babij, S. H. Reeder, S. D. Hogan, and D. B. Cassidy, Precision microwave spectroscopy of the positronium $2^3S_1 \rightarrow 2^3P_2$ interval, *Phys. Rev. Lett.* **131**, 043001 (2023).
- [41] M. Doser *et al.* (AEGIS Collaboration), Exploring the WEP with a pulsed cold beam of antihydrogen, *Classical Quantum Gravity* **29**, 184009 (2012).
- [42] M. Volponi (AEGIS Collaboration), Weighing antimatter: AEGIS Phase 2, upgrades and first data, *Nuovo Cimento C* **46**, 106 (2023).
- [43] S. D. Bass, S. Mariuzzi, P. Moskal, and E. Stepien, Colloquium: Positronium physics and biomedical applications, *Rev. Mod. Phys.* **95**, 021002 (2023).
- [44] A. Soleimani Dorcheh and M. Abbasi, Silica aerogel; synthesis, properties and characterization, *J. Mater. Process. Technol.* **199**, 10 (2008).
- [45] F. Akhter, S. Soomro, and V. Inglezakis, Silica aerogels; A review of synthesis, applications and fabrication of hybrid composites, *J. Porous Mater.* **28**, 1387 (2021).
- [46] S. P. Patil, V. G. Parale, H.-H. Park, and B. Markert, Mechanical modeling and simulation of aerogels: A review, *Ceram. Int.* **47**, 2981 (2021).
- [47] B. Hosticka, P. Norris, J. Brenizer, and C. Daitch, Gas flow through aerogels, *J. Non-Cryst. Solids* **225**, 293 (1998).
- [48] K. S. Khaw, A. Antognini, T. Prokscha, K. Kirch, L. Liskay, Z. Salman, and P. Crivelli, Spatial confinement of muonium atoms, *Phys. Rev. A* **94**, 022716 (2016).
- [49] A.-M. El-Sayed, Y. Wimmer, W. Goes, T. Grasser, V. V. Afanas'ev, and A. L. Shluger, Theoretical models of hydrogen-induced defects in amorphous silicon dioxide, *Phys. Rev. B* **92**, 014107 (2015).
- [50] A. V. Dolbin, M. V. Khlistyuck, V. B. Esel'son, V. G. Gavrilko, N. A. Vinnikov, R. M. Basnukaeva, V. E. Martsenuk, N. V. Veselova, I. A. Kaliuzhnyi, and A. V. Storozhko, Sorption of hydrogen by silica aerogel at low-temperatures, *Low Temp. Phys.* **44**, 144 (2018).
- [51] S. Zeng, A. Hunt, and R. Greif, Transport properties of gas in silica aerogel, *J. Non-Cryst. Solids* **186**, 264 (1995), proceedings of the Fourth International Symposium on AEROGELS.
- [52] Y. Yue, J. Wang, Y. Zhang, Y. Song, and X. Zuo, Interactions of atomic hydrogen with amorphous SiO_2 , *Physica (Amsterdam)* **533B**, 5 (2018).
- [53] S. Agostinelli *et al.* (GEANT4 Collaboration), GEANT4—a simulation toolkit, *Nucl. Instrum. Methods Phys. Res., Sect. A* **506**, 250 (2003).
- [54] J. Allison *et al.*, GEANT4 developments and applications, *IEEE Trans. Nucl. Sci.* **53**, 270 (2006).
- [55] J. Allison *et al.*, Recent developments in GEANT4, *Nucl. Instrum. Methods Phys. Res., Sect. A* **835**, 186 (2016).
- [56] J.-K. Chen, B.-Y. Hu, X.-B. Ji, Q.-M. Ma, J. Tang, Y. Yuan, X.-M. Zhang, Y. Zhang, W.-W. Zhao, and W. Zheng, Application of a supercomputer Tianhe-II in an electron-positron collider experiment BESIII, *J. Instrum.* **18**, T03003 (2023).
- [57] Y. Xu, Y. Ning, Z. Qin, Y. Teng, C. Feng, J. Tang, Y. Chen, Y. Fukao, S. Mihara, and K. Oishi, Development of a SciFi-based beam monitor for COMET, [arXiv:2308.15253](https://arxiv.org/abs/2308.15253).